

ON THE FORMATION AND EVOLUTION OF COMMON ENVELOPE SYSTEMS

FREDERIC A. RASIO¹

Department of Physics, MIT 6-201, Cambridge, MA 02139; rasio@mit.edu

AND

MARIO LIVIO

Space Telescope Science Institute, 3700 San Martin Drive, Baltimore, MD 21218; mlivio@stsci.edu

Received 1995 November 15; accepted 1996 May 31

ABSTRACT

We discuss the formation of a common envelope system following dynamically unstable mass transfer in a close binary and the subsequent dynamical evolution and final fate of the envelope. We base our discussion on new three-dimensional hydrodynamic calculations that we have performed for a close binary system containing a $4 M_{\odot}$ red giant with a $0.7 M_{\odot}$ main-sequence star companion. The initial parameters are chosen to model the formation of a system resembling V471 Tau, a typical progenitor of a cataclysmic variable binary. The calculations are performed using the smoothed particle hydrodynamics (SPH) method with up to 5×10^4 particles. As initial condition we use an exact hydrostatic equilibrium configuration at the onset of dynamically unstable mass transfer. The nonlinear development of the instability is followed using SPH until a quasi-static common envelope configuration is formed. In our highest resolution calculation, we find evidence for a corotating region of gas around the central binary. This is in agreement with the theoretical model proposed by Meyer & Meyer-Hofmeister for the evolution of common envelope systems, in which this central corotating region is coupled to the envelope through viscous angular momentum transport only. We also find evidence that the envelope is convectively unstable, in which case the viscous dissipation time could be as short as ~ 100 dynamical times, leading to rapid ejection of the envelope. For V471 Tau our results, and the observed parameters of the system, are entirely consistent with rapid envelope ejection on a timescale ~ 1 yr and an efficiency parameter $\alpha_{\text{CE}} \simeq 1$.

Subject headings: hydrodynamics — instabilities — stars: binaries: close — stars: evolution — stars: interiors

1. INTRODUCTION AND MOTIVATION

Common envelope (CE) evolution is thought to be the consequence of a dynamical mass transfer event in a close binary system. A dynamical mass transfer instability can occur when mass is being transferred from the more massive to the less massive component and the mass donor has a deep convective envelope, as in the case of a giant or asymptotic giant branch (AGB) star losing mass to a less massive companion. When these conditions are realized, the mass-losing star is usually unable to contract as rapidly as its Roche lobe, and thus it starts transferring mass on a dynamical timescale. Typically under such conditions, the secondary is unable to accrete all the proffered mass, and it is driven out of thermal equilibrium. The system is then expected to quickly reach a configuration in which the core of the evolved star and the companion are orbiting each other inside a common envelope of gas which is not corotating with the binary (see recent reviews by Webbink 1988; Iben & Livio 1993; Livio 1996).

The main effect of the CE phase is expected to be a substantial reduction in the separation of the binary, possibly accompanied by the ejection of the entire envelope. The concept of CE evolution, as described above, was introduced by Paczyński (1976) to explain the formation of cataclysmic variables and by Ostriker (1975) in the context of massive X-ray binaries. It is now thought that all binary systems containing at least one compact component and with orbital periods shorter than a few days (this includes most cataclysmic variables, binary pulsars, and X-ray

binaries) must have gone through a common envelope phase (except perhaps in dense cluster environments, where close stellar encounters can operate). It is not surprising, therefore, that this topic has received considerable attention in recent years and has been the subject of many theoretical studies (de Kool 1987, 1990; Livio & Soker 1988; Terman, Taam, & Hernquist 1994, 1995 and references therein). Most of these theoretical studies have focused on the final stages of the CE evolution in an attempt to determine the orbital parameters of the emerging binary (Taam & Bodenheimer 1991; Taam, Bodenheimer, & Rozyczka 1994; Yorke, Bodenheimer, & Taam 1995). However, the treatment of the formation and early dynamical evolution of CE systems has been extremely crude until now. For example, a fictitious drag force was applied to trigger the initial spiral-in in the calculation of Terman et al. (1994), and the secondary was placed directly inside the envelope of the primary in Terman et al. (1995).

There are several reasons why it is important to study this early phase of CE evolution. (1) This is the only phase in the life of a CE system that can be modeled in a realistic way. Indeed, current three-dimensional hydrodynamic codes can only follow reliably the *dynamical phase* of the evolution. The later stages depend crucially on angular momentum and energy transport processes that are difficult to model and take place on dissipation timescales, which can be many orders of magnitude longer than the dynamical time. (2) It is clear that an accurate calculation of the early dynamical phase is required in order to establish the *initial conditions* of separate calculations for the dissipative phase. Attempts to predict the final outcome of a CE phase

¹ Alfred P. Sloan Foundation Fellow.

based on the efficiency parameter for energy deposition α_{CE} (Livio & Soker 1988) give results that depend critically on the assumptions made about these initial configurations. Indeed, because of the uncertainty in the initial configuration (and the ambiguity in estimating its binding energy), various definitions of α_{CE} , e.g., in Iben & Tutukov (1984) and de Kool (1990), can give results that differ by as much as a factor ~ 10 (Yungelson, Tutukov, & Livio 1993). (3) In some cases it is possible that the complete ejection of the envelope could occur on a timescale not much longer than the dynamical time (say ~ 100 dynamical times). In such a case, a purely dynamical calculation can in fact provide a complete description of the CE phase.

In this paper, we present the results of new hydrodynamic calculations in three dimensions for the unstable mass transfer in a close binary and the early dynamical evolution of a CE system. The calculations are done for a binary containing a red giant with a less massive main-sequence star companion, representing a typical progenitor of a precataclysmic-variable system. The initial conditions for these calculations are carefully constructed equilibrium configurations for the close binary at the onset of dynamically unstable mass transfer. In § 2 we review our numerical method, smoothed particle hydrodynamics (SPH) and describe how to construct equilibrium configurations for close binaries in three dimensions. In § 3 we present the results of our dynamical calculations and discuss their dependence on the numerical resolution. Some speculations about the final fate of the CE system and a summary of the main results follow in § 4.

2. NUMERICAL METHOD

2.1. The Smoothed Particle Hydrodynamics Code

The smoothed particle hydrodynamics (SPH) method has been used for the calculations presented here. SPH is a Lagrangian method used to treat astrophysical problems involving self-gravitating fluids moving freely in three dimensions (see Monaghan 1992 for a recent review). Our SPH code was developed originally by Rasio (1991) specifically for the study of close stellar interactions (Rasio & Shapiro 1991, 1992). The implementation of the SPH scheme is similar to that adopted by Hernquist & Katz (1989), but the gravitational field is calculated using a fast grid-based fast Fourier transform (FFT) solver. The neighbor searching is performed using a multigrid hierarchical version of the linked-list method usually adopted in P^3M particle codes (Hockney & Eastwood 1988). Other details about the implementation, as well as a number of test-bed calculations using our SPH code for binary systems are presented in the above references.

The highest resolution calculation presented here was done using $N = 5 \times 10^4$ SPH particles, and each particle interacting with a nearly constant number of neighbors $N_N \simeq 60$. The gravitational potential is calculated by FFT on a 256^3 grid. With these resources, a complete calculation, starting from the onset of mass transfer and ending with the formation of a quasi-static CE configuration, takes about 250 CPU hours on an IBM SP-2 supercomputer.

We use a constant number density of SPH particles with varying particle masses to construct the initial conditions. This is done in order to maintain good spatial resolution and mass resolution near the stellar surface, which is particularly important for problems involving tidal interactions

and mass transfer in close binaries. We use a simple ideal gas equation of state with $P = A\rho^{5/3}$, where P is the pressure, ρ is the density, and $A \propto \exp s$ is a function of the local specific entropy s . Our implementation of SPH uses A as a fundamental variable and integrates an evolution equation for entropy rather than energy (Rasio & Shapiro 1992). Shocks are the only source of entropy production in these calculations, and we use the standard SPH artificial viscosity to treat them.

2.2. Conventions and Choice of Units

We consider a binary system containing a red giant primary and a main-sequence secondary. The primary has a mass $M_1 = 4 M_\odot$. The red giant is modeled as a compact core plus an extended envelope with a mass ratio $M_{\text{core}}/M_{\text{env}} = \frac{1}{5}$, i.e., $M_{\text{core}} \simeq 0.7 M_\odot$ and $M_{\text{env}} \simeq 3.3 M_\odot$. The mass of the secondary is $M_2 = M_{\text{core}} \simeq 0.7 M_\odot$. Both the secondary and the red giant core are modeled as point masses interacting with the gas through gravity only. Close to the point masses, the gravitational field is smoothed over a length h_c comparable to the local SPH smoothing length. Specifically, we treat the core and the secondary as uniform-density spheres of radius h_c when computing their gravitational interaction with an SPH particle. Typically we have $h_c/R_1 \sim 10^{-2}$, where R_1 is the radius of the red giant envelope. The gravitational interaction between the two point masses themselves is not smoothed. Initially the envelope of the red giant is assumed to have constant specific entropy, i.e., we let $A = \text{constant}$ for all SPH particles at $t = 0$.

Throughout this paper, numerical results are given in units $G = M_{\text{env}} = A = 1$, where G is the gravitational constant, M_{env} is the total mass of gas in the system (initially inside the red giant envelope), and A is the (constant) entropy variable at $t = 0$. In these units, the binary separation at $t = 0$ (onset of mass transfer) is $r_i \simeq 2.9$, and the radius of the red giant is $R_1 \simeq 1.8$. The units of time, velocity, and density are then

$$t_0 \simeq 2 \text{ days} \times \left(\frac{r_i}{100 R_\odot} \right)^{3/2} \left(\frac{M_{\text{env}}}{3.3 M_\odot} \right)^{-1/2}, \quad (1)$$

$$v_0 \simeq 140 \text{ km s}^{-1} \times \left(\frac{r_i}{100 R_\odot} \right)^{-1/2} \left(\frac{M_{\text{env}}}{3.3 M_\odot} \right)^{1/2}, \quad (2)$$

$$\rho_0 \simeq 5 \times 10^{-4} \text{ g cm}^{-3} \times \left(\frac{r_i}{100 R_\odot} \right)^{-3} \left(\frac{M_{\text{env}}}{3.3 M_\odot} \right). \quad (3)$$

2.3. Constructing the Initial Condition

In addition to its normal use for dynamical calculations, SPH can also be used to construct highly accurate hydrostatic equilibrium configurations in three dimensions (Rasio & Shapiro 1994, 1995). We consider only *synchronized* binary configurations in this paper. This is a reasonable assumption for a system with moderate mass ratio, and we have checked that the synchronized configuration we construct at $t = 0$ is indeed tidally stable (although marginally). Binary systems with more extreme mass ratios can never reach a stable synchronized configuration and in such a case an initial condition containing a nonspinning primary may be more realistic (see, e.g., Rasio 1996 and references therein).

For a synchronized system, the entire mass of fluid is in uniform rotation and equilibrium solutions can be con-

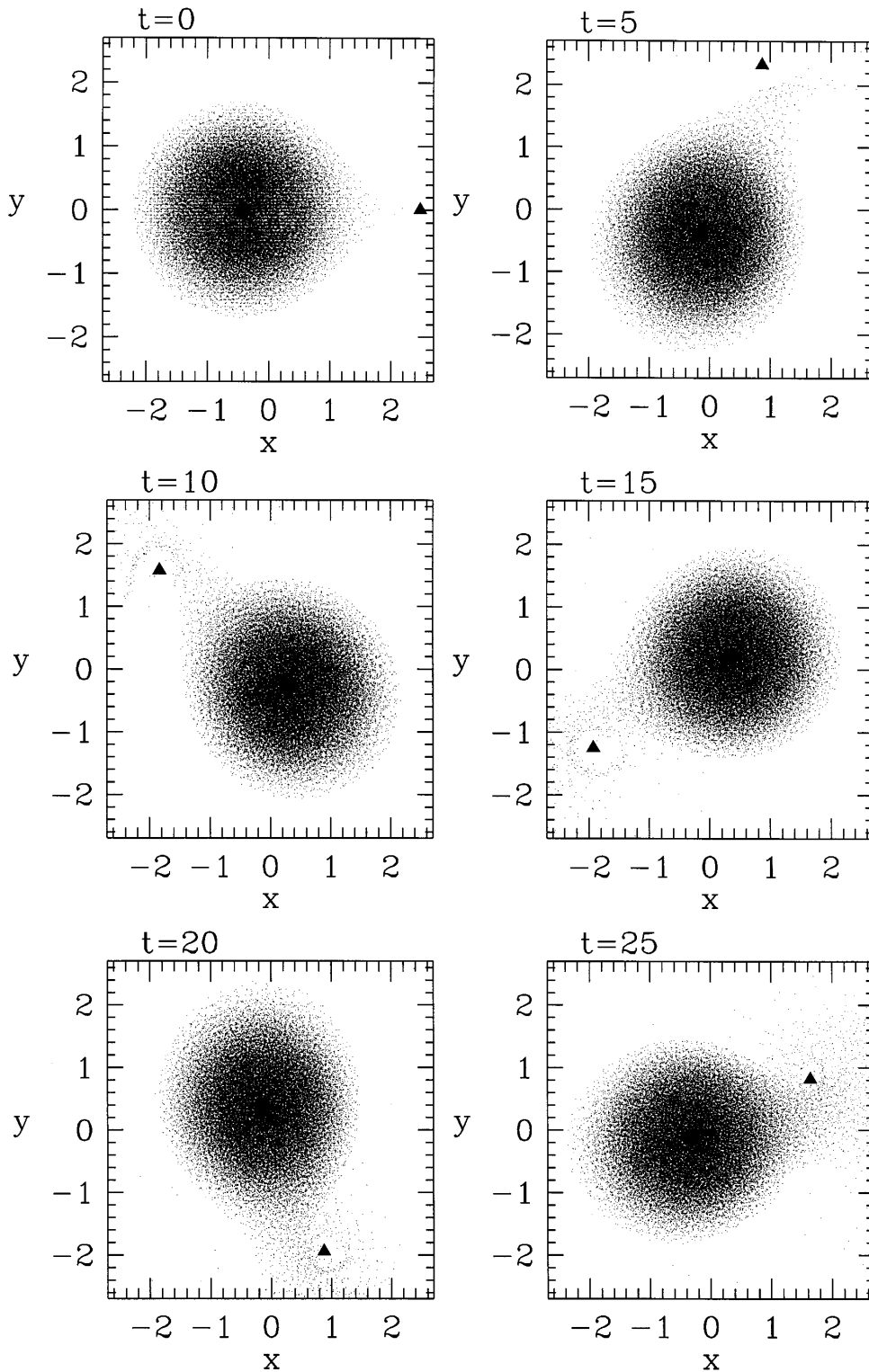


FIG. 1.—Particle plots showing the evolution of the system from the onset of unstable mass transfer to the formation of the common envelope. Projections of all SPH particles onto the orbital (x, y) plane of the binary are shown at various times. The origin is at the center of mass of the system. Units are defined in § 2.2. The core of the red giant is marked by a large round dot, the companion by a triangle. Both are treated as point masses in the calculation, but their gravitational interaction with the gas is softened over a distance roughly comparable to the size of the symbols in these plots. The orbital rotation is counterclockwise. At $t = 0$ the system is in a synchronized hydrostatic equilibrium configuration with just a few SPH particles outside the critical Roche lobe of the primary. By $t \simeq 20$ the mass transfer flow is well established, and the orbit is decaying unstably. From $t \simeq 30$ to $t \simeq 50$ the companion quickly spirals in through the envelope and the common envelope system is formed. The calculation ends when the separation between the two point masses becomes comparable to the local SPH smoothing length (also comparable to the gravitational smoothing length).

constructed by simply adding a linear friction term $-v/t_{\text{relax}}$ to the Euler equations of motion in the corotating frame. This forces the fluid to relax to a minimum-energy state. We use $t_{\text{relax}} = 1$ in our units, which makes the damping of

unwanted oscillations nearly critical and optimizes the computation time to converge toward an equilibrium. Initially, a spherical envelope of constant specific entropy and density is used for the red giant, and the two stars are placed

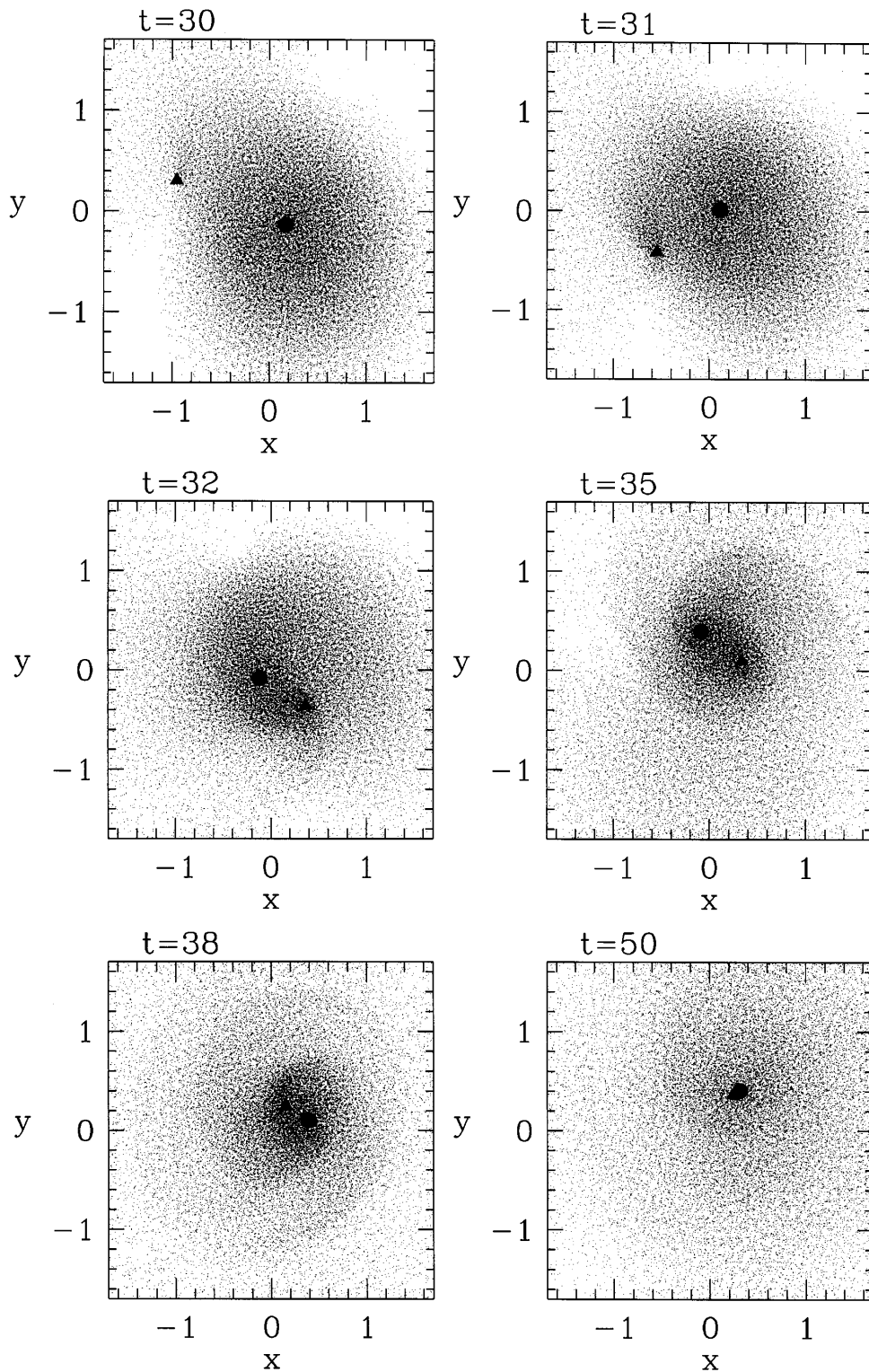


FIG. 1—Continued

at a large separation $r \simeq 4R_1$. While the relaxation takes place, the particle entropies are maintained constant and their positions are continuously adjusted (by a simple uniform translation along the binary axis) so that the separation between the two centers of mass remains constant. Simultaneously, the angular velocity Ω defining the corotating frame is continuously updated so that the net centrifugal and gravitational accelerations of the two centers of mass cancel exactly. With large enough numbers of SPH particles ($N \sim 10^4$ – 10^5), very accurate equilibrium

solutions can be constructed using this relaxation technique, with the virial theorem satisfied to an accuracy of about one part in 10^3 , and excellent agreement found with analytic solutions. In addition, stable equilibrium configurations can be maintained accurately during dynamical integrations lasting up to ~ 100 dynamical times (Rasio & Shapiro 1994, 1995).

In order to construct an initial condition corresponding to the onset of mass transfer, the separation r between the centers of mass during the relaxation calculation is is

decreased very slowly (on a timescale much longer than t_{relax}) so that an entire equilibrium *sequence* is constructed in a single integration. In practice, we let $r(t) = r(0) - t/t_{\text{scan}}$, where $r(0)$ corresponds to well-separated components and $t_{\text{scan}} = 100$ in our units. Using this procedure, we can determine precisely the Roche limit configuration (equilibrium configuration with minimum r) simply by observing the moment when the first few SPH particles begin drifting across the inner Lagrangian point onto the secondary (Rasio & Shapiro 1995). This Roche limit configuration, corresponding to the onset of mass transfer, is then used as an initial condition for a dynamical integration.

A particle plot corresponding to the initial Roche limit configuration is shown in Figure 1 ($t = 0$). The large tidal distortion of the envelope near the axis is evident, and there are just a few particles that have crossed the inner Lagrangian point.

3. RESULTS

3.1. Initial Spiral-in

Soon after the beginning of mass transfer, a thick torus of material forms around the secondary ($t \approx 10$ – 20). As the initial stream leaving the primary is compressed rapidly in a convergent flow and later self-intersects at a highly supersonic speed, the gas is strongly shocked and the torus expands rapidly and thickens, leading to a radial outflow around the secondary in addition to the beginning of an accretion flow (cf. Sawada, Matsuda, & Hachisu 1986). The mass transfer rate increases rapidly, on a timescale comparable to the orbital period. Two factors contribute to making the mass transfer dynamically unstable here (for general discussions of unstable mass transfer, see Hjellming & Webbink 1987; Hjellming 1989; Hut & Paczyński 1984). First, as the red giant primary loses mass, the isentropic envelope responds adiabatically by expanding. Second, since the mass transfer is from the more massive to the less massive component, and since angular momentum is lost from the orbit, the orbital separation tends to decrease. The two effects combine to make Roche lobe overflow accelerate catastrophically on a dynamical timescale. By $t \approx 30$, the companion is entering the dense outer layers of the red giant envelope and will then plunge in almost radially.

In this dynamical calculation, the spiral-in phase is very brief, taking just about one orbital period. This is because we start the calculation when a dynamically significant amount of mass is already being transferred. In reality, of course, this phase is expected to be much longer, as the Roche lobe eats slowly into the outer atmosphere of the primary (e.g., Webbink 1984).

Figure 2 shows the evolution of the separation between the two point masses during the entire calculation. The orbital decay is very slow at first, but accelerates catastrophically around $t \approx 30$. As soon as it enters the denser region of gas inside the red giant envelope, the companion sinks relatively quickly into the deep interior of the envelope, with the separation decreasing to about half a stellar radius by $t \approx 32$. This phase of the evolution is characterized by a much stronger dynamical interaction between the companion and the entire mass of gas in the system.

3.2. Strong Dynamical Interaction

The motion of the companion inside the envelope is largely supersonic, especially in the outer layers where large

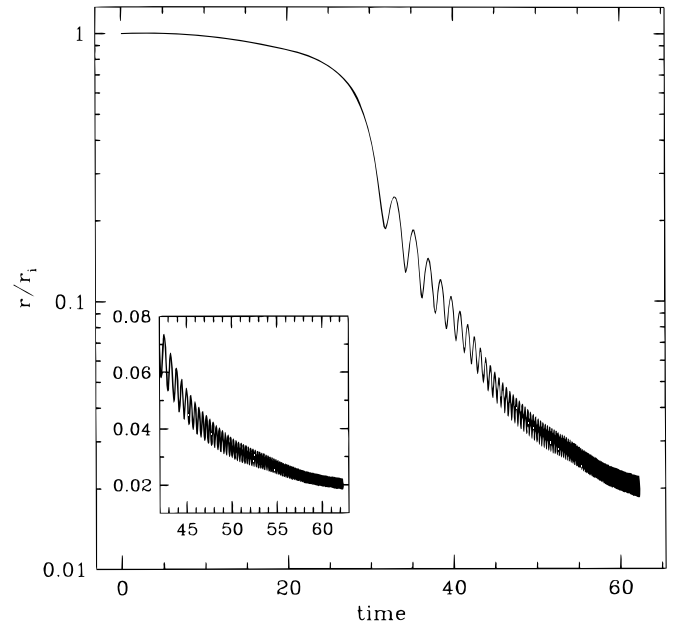


FIG. 2.—Time evolution of the separation between the two point masses in the calculation. In the insert we show the details of the evolution near the end of the calculation, on a linear scale. The separation is given here in units of the initial binary separation r_i , while time is in the units defined in § 2.2.

Mach numbers are reached. As a result, during the initial phase of the radial plunge, strong dissipation occurs in a simple bow-shock structure behind the companion. This is illustrated in Figure 3, which shows regions of high and low entropy in the gas. Here we use $A > 2$ to separate the “high-entropy” particles. Recall that all particles have $A = 1$ at $t = 0$. In our units, a change of order unity in A over a distance of order unity corresponds to a buoyancy force comparable to gravity [i.e., $dA/dr \sim 1$ gives a Brunt-Väisälä frequency comparable to the local dynamical frequency $(G\rho)^{-1/2}$]. By $t \approx 35$, however, the red giant core itself has been displaced away from its original position at the center of the envelope, and the two point masses are now truly orbiting one another inside a common gravitational potential well. The dissipation process becomes much more complex at this point (Figs. 3c and 3d), with several interacting spiral shock fronts propagating out. These spiral shocks provide the basic coupling mechanism between the gas and the binary at the beginning of this strongly dynamical phase of the evolution, while viscous dissipation becomes dominant near the end (see below).

It is during this phase of strong dynamical interaction between the two point masses and the gas that a large redistribution of energy and angular momentum takes place in the system. Figures 4 and 5 show the transfer of energy and angular momentum from the orbital motion to the gas during the dynamical evolution. Note that the “orbital” energy and angular momentum shown here are those associated with the motion of the two point masses (i.e., the core of the red giant and the secondary). This is an appropriate definition at late times, when the common envelope has already formed, but not at early times ($t \lesssim 20$), when most of the gas is still bound to the red giant core. This ambiguity in separating “orbital” from “envelope” quantities also affects the definition of the efficiency parameter α_{CE} (cf. § 4.1). The exact values of the orbital energy and

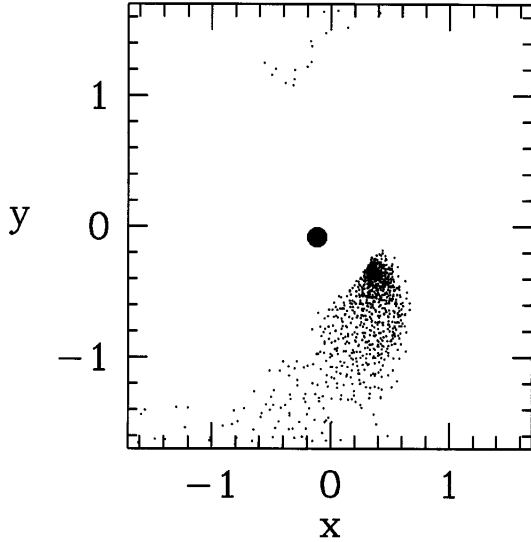


FIG. 3a

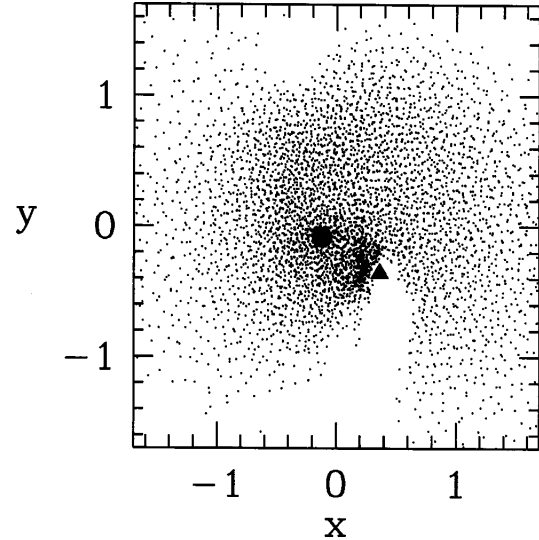


FIG. 3b

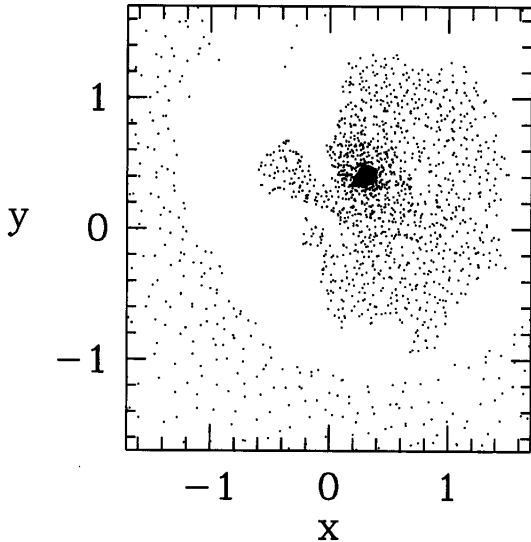


FIG. 3c

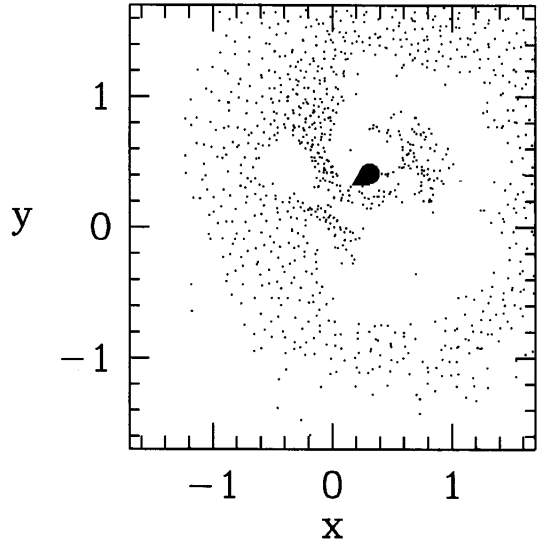


FIG. 3d

FIG. 3.—Particle plots showing regions of high and low entropy in the gas near the equatorial plane ($|z| < 0.1$). All fluid particles have $A = P/\rho^{5/3} = 1$ at $t = 0$. The left and right plots show particles with $A > 2$ (high entropy) and $A < 2$ (low entropy), respectively. In (a) and (b) we show the simple bow-shock structure behind the companion in the early phase of the radial plunge (here for $t = 32$; see the corresponding plot in Fig. 1). In (c) and (d) a more complex structure is seen ($t = 50$), following the displacement of the red giant core and the interactions between various spiral shock fronts.

angular momentum at $t = 0$ are $E_{\text{orb}} = -GM_1 M_2/(2r_i) \simeq -0.044$ and $J_{\text{orb}} = M_1 M_2 [Gr_i/(M_1 + M_2)]^{1/2} \simeq 0.37$.

We see in Figure 4 that the energy transfer rate appears approximately constant during the entire phase of strong dynamical interaction ($t \gtrsim 30$). Instead, the orbital angular momentum (Fig. 5) is lost mostly during the initial spiral-in and the first radial plunge but then becomes approximately constant for $t \gtrsim 35$. By the end of the calculation, essentially all of the angular momentum in the system has been transferred to the gas. Initially, most of the binding energy in the system is in the red giant envelope. By the end of the calculation, most (but not all) of the binding energy is in the binary system. Linear momentum is also exchanged between the gas and point masses and, since the gas ejection is not isotropic, the binary receives a small recoil velocity v_{rec} . At the end of our calculation we find $v_{\text{rec}} \simeq 0.054$ in our

units, which corresponds to $v_{\text{rec}} \simeq 8 \text{ km s}^{-1}$ for a typical system.

3.3. The Common Envelope Configuration

An important question concerns the motion of the gas in the immediate vicinity of the binary system after the formation of the common envelope. In our highest resolution calculation, we find that a corotating region of gas forms at the center of the common envelope. The corotating gas is concentrated near the orbital plane. This is illustrated in Figure 6, which shows the distribution of SPH particles in the (Ω, r_{cyl}) plane at $t = 40$. Here $\Omega = v_t/r_{\text{cyl}}$, where v_t is the component of the particle velocity in the azimuthal direction and r_{cyl} is the distance to the rotation axis (vertical axis passing through the center of mass of the binary). Both the equatorial radius and the vertical thickness of the corotat-

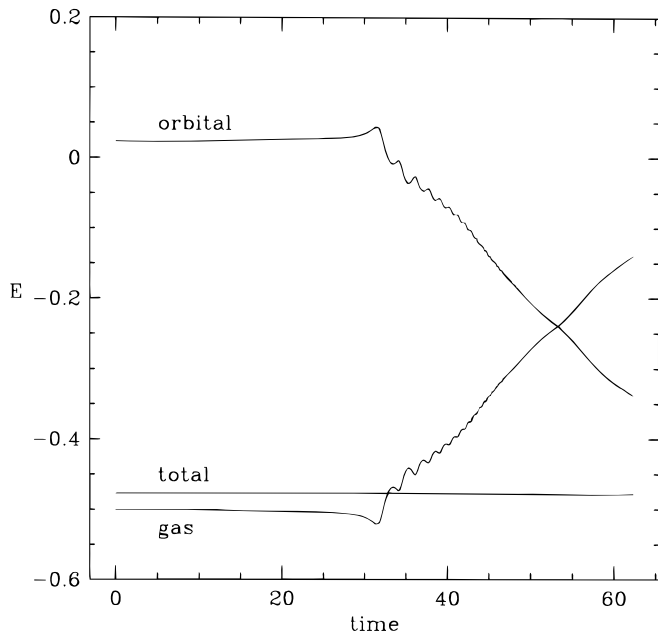


FIG. 4.—Time evolution of various energies in the system. The orbital energy is that associated with the two point masses only (note that this is not equal to the orbital energy of the binary system at $t = 0$ since the primary also contains all the gas at that time). The gas energy is the sum of the kinetic, thermal, and self-gravitational energies associated with all SPH particles, plus the potential energy of the (softened) gravitational interaction between the SPH particles and the two point masses. The total (conserved) energy is then the sum of the gas and orbital energies.

ing region are roughly comparable to the binary separation. This corotating region continues to exist and remains well resolved until the end of our highest resolution calculation (but see § 3.4 below).

At the end of our calculation ($t \approx 62$), most of the mass in the common envelope has relaxed to a quasi-static equilibrium. The value of the virial ratio for the bound gas is

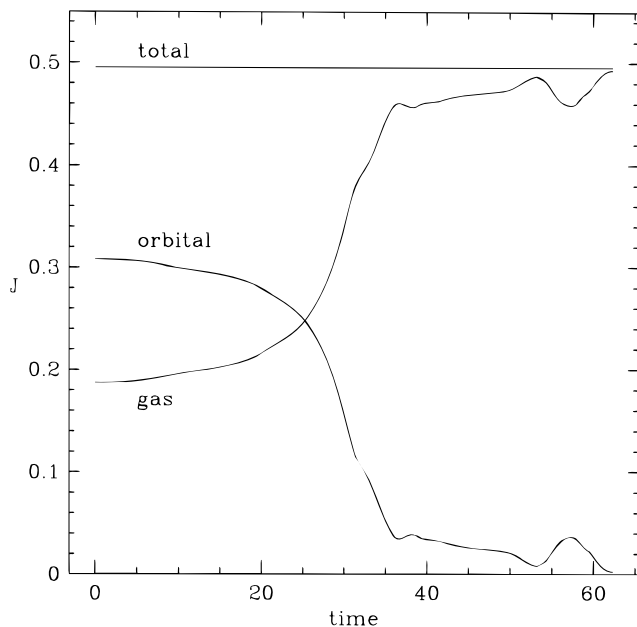


FIG. 5.—Time evolution of the angular momentum in the system. The orbital angular momentum is that associated with the motion of the two point masses only, while the gas angular momentum corresponds to the motion of all SPH particles.

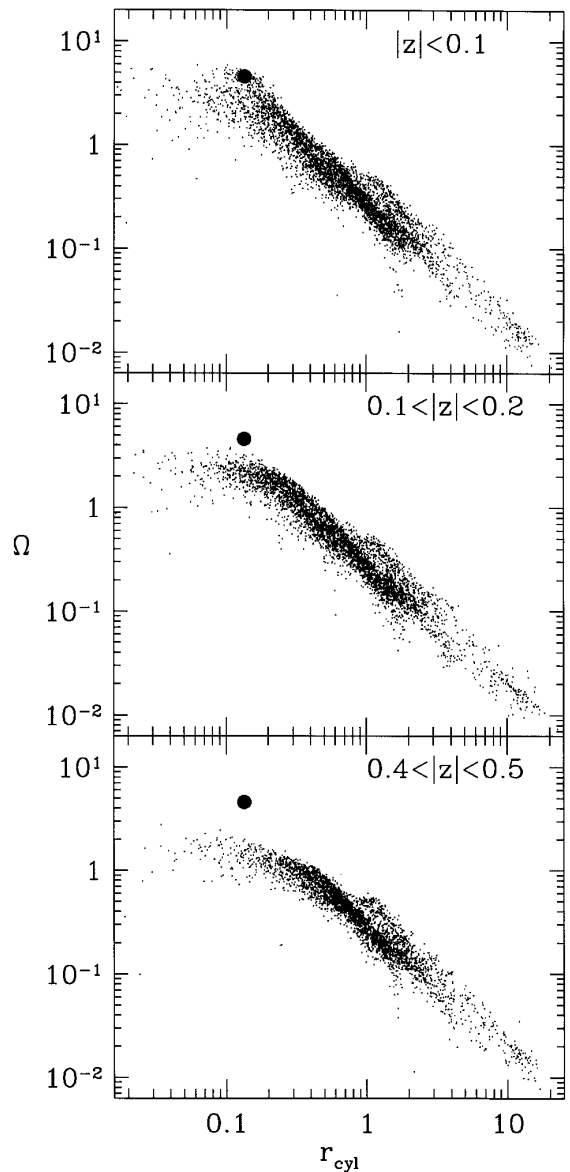


FIG. 6.—Angular velocity profiles in the common envelope at $t = 40$. The large dot indicates the position of the two orbiting point masses. The lighter dots show the positions of individual SPH particles. The three plots correspond to horizontal slices (perpendicular to the rotation axis) progressively further away from the equatorial (symmetry) plane $z = 0$. Clearly, a corotating region of gas exists close to the binary system near $z = 0$.

$|2T + W + 2U|/|W| \approx 0.01$, where T is the kinetic energy, W is the gravitational potential energy, and U is the internal energy (this dimensionless virial ratio would be zero in strict hydrostatic equilibrium). The envelope is rapidly rotating, with $T/|W| \approx 0.11$, not far from the secular stability limit at $T/|W| \approx 0.14$ (e.g., Tassoul 1978). The mass-loss fraction can be determined using the method of Rasio & Shapiro (1991) based on the specific binding energy and enthalpy of each individual particle. Using this method we find that about 10% of the total mass of gas has become unbound by the end of the calculation (but see the discussion in § 4.1 below). The final density ρ , specific entropy $A = P/\rho^{5/3}$, and specific angular momentum $j = r_{\text{cyl}} v_t$ inside the common envelope are shown in Figure 7 as a function of the interior mass fraction m/M . The quantities shown have been mass-averaged over cylindrical shells cen-

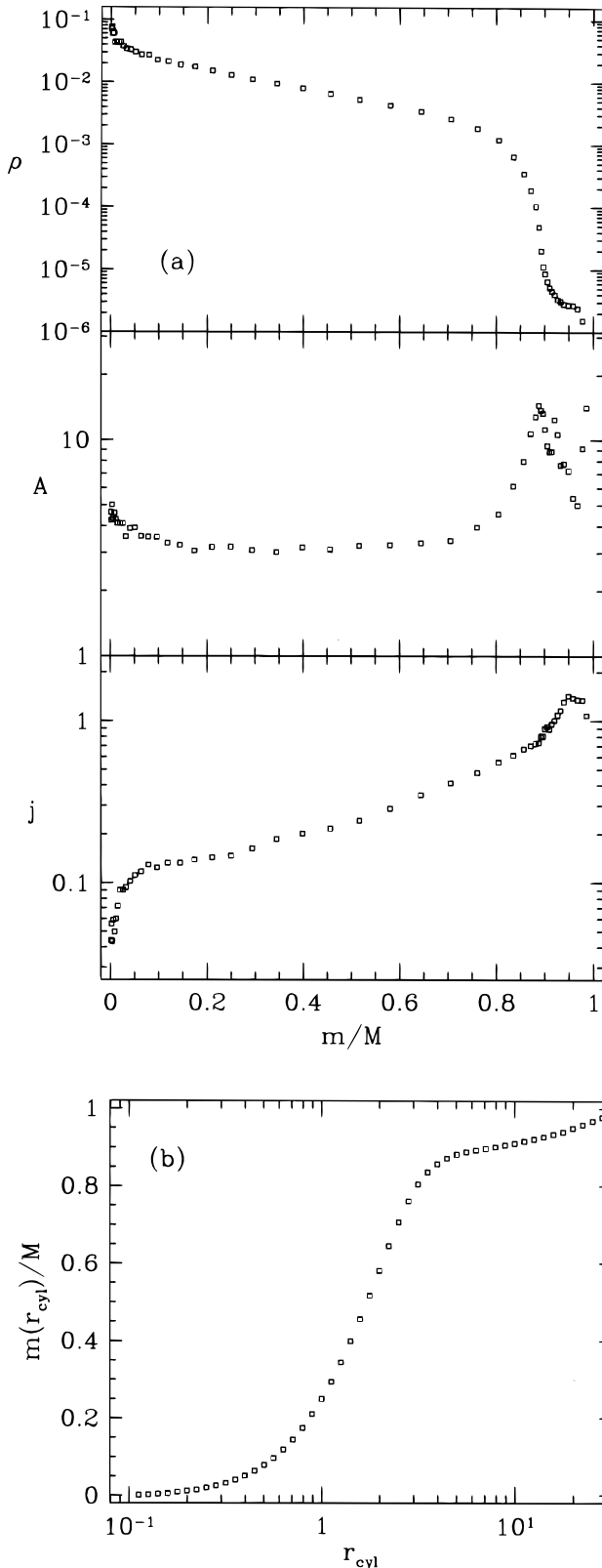


FIG. 7.—Average density (ρ), specific entropy ($A = P/\rho^{5/3}$), and specific angular momentum ($j = r_{\text{cyl}}v_\phi$) profiles in the common envelope at the end of the calculation. Here m/M is the gas mass fraction interior to a cylindrical surface centered on the rotation axis ($m/M = 0$ at the center and $m/M = 1$ at the outer surface) and r_{cyl} is the distance to the rotation axis.

tered on the rotation axis. The correspondence between the interior mass fraction m/M and the radius r_{cyl} of a cylinder is also shown (Fig. 7b). The outermost $\sim 10\%$ of the mass is

unbound. For the bound gas, the specific angular momentum increases with r_{cyl} as required for dynamical stability (e.g., Tassoul 1978).

The specific entropy of the bound gas is nearly constant or increasing everywhere except near the center, close to the binary, where it decreases outward. This is a clear sign that *most of the envelope is or has been dynamically unstable to convection*. The specific entropy profile left behind by the dynamical interaction between the shrinking binary and the envelope has $dA/dr_{\text{cyl}} < 0$. Convective (Rayleigh-Taylor) instabilities then develop, redistributing the material so that a nearly constant specific entropy profile is obtained. Close to the binary, however, the convective motions have not yet had the time to develop, and an unstable entropy gradient is still seen. Careful examinations (e.g., using computer animations) of the fluid motions in the inner envelope do indeed reveal the presence of convective motions. On a dynamical timescale, and with the fairly coarse spatial resolution of a three-dimensional calculation, these convective motions take the form of large bubbles of higher entropy gas rising through a region of lower entropy gas that surrounds them. A clear example of such a rising high-entropy bubble (by far the largest observed in this calculation) is visible to the left of the binary in the particle plot of Figure 3c (and Fig. 3d). Such large inhomogeneities in the gas near the center also produce torques on the binary, leading to the somewhat irregular variation of the angular momentum near the end of the calculation (Fig. 4, $t > 50$).

3.4. Dependence of the Results on the Numerical Resolution

Our SPH calculations of the CE evolution must be terminated when the separation between the two inner cores becomes comparable to the local spatial resolution in the central region of gas. Otherwise the interaction between the orbital motion and the gas can no longer be treated correctly. The conditions at the end of our highest resolution run are illustrated in Figure 8.

In a calculation with a smaller number of particles one may be tempted to continue past this point. This may be necessary for the gas to reach a quasi-steady state at the end of the calculation. However, misleading results can then be obtained. Most importantly for this problem, the motion of the gas in the vicinity of the binary system at the end of the calculation will be corrupted by the loss of spatial resolution there. If we repeat the same calculation as above with $N = 8000$ particles (which decreases the spatial resolution by a factor ~ 2), and integrate until the same final binary separation is reached, we no longer find that the gas is corotating with the binary at the end. This is shown in Figure 9, where we compare the final rotation profiles for the two calculations. The reason is simply that all SPH particles within a region of size $\sim \langle h \rangle$ close to the center (where $\langle h \rangle$ is the average SPH smoothing length in that region) must necessarily have comparable values of Ω . Therefore, the true angular velocity profile near the center of any rapidly rotating configuration will always be truncated at some distance $r_{\text{cyl}} \sim \langle h \rangle$ inside which Ω will appear nearly constant. In Figure 9, we see that, with a lower resolution calculation, we would have concluded incorrectly that the angular velocity of the binary is ~ 10 times larger than that of the gas near the center of the final configuration.

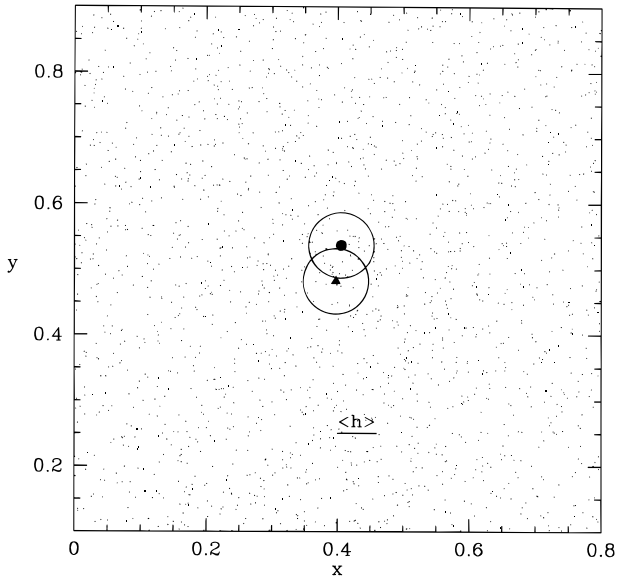


FIG. 8.—Particle plot showing the region of gas close to the binary system at the end of the calculation. The two large circles indicate the extent of the regions where the gravitational interaction between the point masses and the gas is smoothed. This is comparable to the average SPH smoothing length $\langle h \rangle$ in this region, also shown.

Having found that the main coupling mechanism between the binary and the gas in the final steady state is viscous transport of angular momentum in the differentially rotating envelope, we must now also ask how accurately this can be represented in numerical calculations. SPH calculations in particular can have large spurious shear viscosity because of the representation of the fluid by discrete particles and because all forms of artificial viscosity

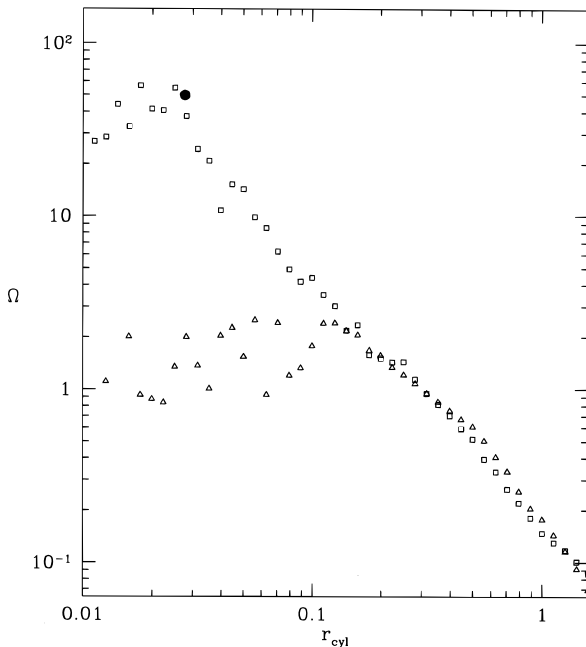


FIG. 9.—Angular velocity profile in the common envelope at the end of two calculations with different spatial resolution. The square dots correspond to our highest resolution calculation, with $N = 5 \times 10^4$ particles, whereas the triangles correspond to a calculation with $N = 8000$. The central corotating region of gas is no longer resolved.

(introduced in the method to treat shocks) also introduce artificial shear viscosity. Extensive tests of SPH using simple experiments with shear flows indicate that the angular momentum transport timescale in differentially rotating envelopes may be typically ~ 100 dynamical times (Lombardi, Rasio, & Shapiro 1996). This is not much longer than the time span of the present calculations, and therefore we expect the numerical viscosity to play a significant role in our results.

Indeed, if, for example, we repeat short segments of the numerical integration around $t = 50$ with different values for the parameters of the artificial viscosity, we find that the value of the energy transfer rate (slope of the curves near $t = 50$ in Fig. 4) changes slightly. If we vary the artificial viscosity parameters over the full range of values that would still lead to a reasonable treatment of shocks (smoothing a simple one-dimensional shock front over a distance $\approx 0.5\langle h \rangle - 5\langle h \rangle$), the energy transfer rate varies by as much as $\sim 50\%$. However, a large effective viscosity may well be present in the real system if, as our results suggest, the initial entropy profile in the envelope as it is created is unstable to convection. Although our three-dimensional calculations cannot resolve the fine details of the convective motions, a large eddy viscosity is expected in this regime. If processes like convection (or perhaps magnetic fields; cf. Regös & Tout 1995) determine the effective viscosity of the envelope in the real system, then we may not be able to calculate the evolution in a quantitatively accurate way (a similar problem arises in models of accretion disks). In that case, a low-resolution but qualitatively reasonable calculation such as the one presented here may be our only resource for developing a theoretical understanding of CE evolution.

4. DISCUSSION

4.1. The Final Fate of the Envelope

Although our dynamical calculations cover only the initial phase of CE evolution, we can speculate about the subsequent evolution of the envelope driven by viscous dissipation. Complete ejection of the envelope may possibly be achieved in a time not much longer than the time covered by our calculations. Indeed, a naive extrapolation of the energy transfer rate shown in Figure 3 would lead to the conclusion that the entire envelope is liberated in a time $t \lesssim 100$, which in our units (see eq. [2]) means $t \lesssim 1$ yr. Similarly, if we look at the mass-loss fraction as a function of time (Fig. 10), a simple extrapolation would predict that all the gas becomes unbound after this time. A direct determination of the envelope ejection time is impossible here because the calculations must be terminated well before a large fraction of the mass has been ejected. In addition, at the end of our calculations, there are large uncertainties in the determination of the gas mass fraction that is likely to become unbound eventually. This is because we cannot predict how much of the enthalpy associated with each fluid particle will be later transformed into kinetic energy of a radial outflow. If we include the enthalpy in the estimate of the binding energy (as done in Rasio & Shapiro 1991), we obtain an upper limit to the mass-loss fraction. If we do not include it we obtain a lower limit. The two estimates differ significantly at the end of our calculations (Fig. 10).

We emphasize here again that the apparently short viscous time in the envelope may be a numerical artefact (cf. § 3.4). However, if the evolution of the CE system indeed

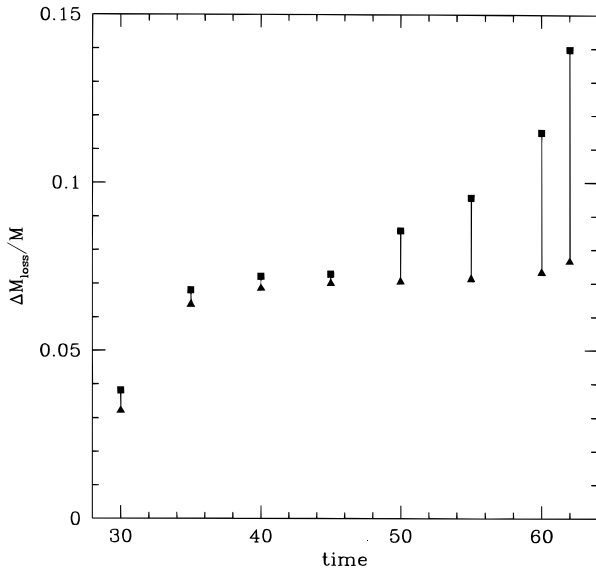


FIG. 10.—Mass-loss fraction $\Delta M_{\text{loss}}/M$ at various times during the strong dynamical interaction phase and at the end of the calculation. The triangles give a lower limit, based on an estimate of the binding energy of each fluid particle that does not include its enthalpy. The squares give an upper limit, assuming that all the enthalpy is eventually transformed into kinetic energy of an outflow.

continues on this short viscous transport time, and if we assume that the binary orbit ceases to evolve when the total gas energy becomes positive, then we can predict the final binary separation simply from conservation of energy (Fig. 4). This gives a final separation $r_f \approx 0.04$ in our units, or $r_f/r_i \approx 1.5 \times 10^{-2}$. This number is in reasonable agreement with the parameters of V471 Tau (which our initial condition is meant to represent), where $r_f \approx 3 R_\odot$ and $r_i \sim 100 R_\odot$ (Iben & Livio 1993). Over such a short time, energy transport processes and radiative losses in the gas are completely negligible, implying that a proper definition of the parameter α_{CE} should give $\alpha_{\text{CE}} \approx 1$ in this case. For comparison, one of the commonly used approximate definitions

$$\frac{(M_1 + M_2)M_{\text{env}}}{2r_i} \approx \alpha_{\text{CE}} M_{\text{core}} M_2 \left(\frac{1}{2r_f} - \frac{1}{2r_i} \right) \quad (4)$$

(Iben & Livio 1993, their eq. [17]) gives $\alpha_{\text{CE}} \approx 0.5$ if we insert $r_f/r_i = 1.5 \times 10^{-2}$ and our values of the masses. Note, however, that equation (4) was derived assuming a rather artificial initial configuration where the two cores are already inside a spherical common envelope of radius r_i . Therefore this expression should only be used for crude order-of-magnitude estimates.

4.2. Summary of Main Results

The calculations presented in this paper cover the *initial dynamical phase* of CE evolution, i.e., a brief episode of unstable mass transfer followed by rapid spiral-in of the companion into the primary and the formation of a CE configuration. For the first time, this dynamical phase of CE evolution has been followed starting from a realistic initial condition. Specifically, we have demonstrated that hydrodynamic calculations can be started from an exact hydrostatic equilibrium solution, representing a close binary system at the onset of unstable mass transfer, and can then follow the evolution through the entire dynamical phase until a quasi-static CE configuration is formed.

Our hydrodynamic calculations can treat only a relatively short evolutionary timescale ($\lesssim 100$ dynamical times, i.e., $\lesssim 1$ yr for a typical system). Consequently, the final CE configuration obtained in the present study could be regarded merely as the initial condition for a potentially slower spiral-in phase, which is regulated by viscous dissipation. The total amount of mass that became unbound during the dynamical phase is only about 10% of the envelope mass. This is to be expected given the short duration of this phase. We have pointed out, however, that an extrapolation of the energy transfer rate obtained in the final stages of our calculation could imply the ejection of the entire envelope on a very short timescale (~ 1 yr) and a high efficiency ($\alpha_{\text{CE}} \approx 1$) of the process. The corresponding reduction in the binary separation would be by a factor $r_i/r_f \sim 100$, which is sufficient to explain the formation of a system like V 471 Tau.

Perhaps our most significant new result is that, during the dynamical phase of CE evolution, a corotating region of gas is established near the central binary. This is done through a combination of spiral shock waves and gravitational torques that can transfer angular momentum from the binary orbit to the gas, and are most effective in the region close to the binary. The corotating region has the shape of an oblate spheroid encasing the binary (i.e., the corotating gas is concentrated in the orbital plane). Our results suggest that the subsequent evolution of the system will be determined by the *viscous coupling between this rigidly rotating inner core and the outer, differentially rotating envelope*. The assumption that rigid rotation will be tidally enforced in a core surrounding the inner binary was already made in the pioneering paper by Meyer & Meyer-Hofmeister (1979). Later, clear indications for such a configuration were obtained with the first two-dimensional numerical calculations of CE evolution (e.g., Sawada, Hachisu, & Matsuda 1984). Although the results of some more recent calculations done in three dimensions (Terman et al. 1994, 1995) appear to indicate that the angular velocity of the gas near the center falls short of corotation, we have pointed out that this may well be the result of insufficient spatial resolution in those calculations.

Accurate calculations of the dissipative phase of CE evolution, including viscous transport of angular momentum and energy transport in the envelope, will be very difficult, given the large uncertainties in our basic understanding of these processes in general. If, however, as our results suggest, the envelope is convective, the effective viscous dissipation rate may be large enough to eject the entire envelope on a timescale as short as ~ 100 dynamical times. In that case, a simple extrapolation of our dynamical results, as mentioned above, may in fact provide a reasonably accurate description of the entire CE evolution.

We thank the Institute of Astronomy at the University of Cambridge for hospitality while this paper was being written. F. A. R. is supported by an Alfred P. Sloan Research Fellowship. M. L. acknowledges support from NASA Grant NAGW-2678. Computations were performed on the IBM SP-2 parallel supercomputer at the Cornell Theory Center, which receives major funding from the NSF and from IBM Corporation, with additional support from the New York State Science and Technology Foundation and members of the Corporate Research Institute.

REFERENCES

- de Kool, M. 1987, Ph.D. thesis, Univ. Amsterdam
 ———. 1990, *ApJ*, 358, 189
 Hernquist, L., & Katz, N. 1989, *ApJS*, 70, 419
 Hjellming, M. S. 1989, Ph.D. thesis, Univ. Illinois
 Hjellming, M. S., & Webbink, R. F. 1987, *ApJ*, 318, 794
 Hockney, R. W., & Eastwood, J. W. 1988, *Computer Simulations Using Particles* (Bristol: Adam Hilger)
 Hut, P., & Paczyński, B. 1984, *ApJ*, 284, 675
 Iben, I. & Tutukov, A. V. 1984, *ApJS*, 54, 335
 Iben, I., Jr., & Livio, M. 1993, *PASP*, 105, 1373
 Livio, M. 1996, *Proc. NATO ASI on Evolutionary Processes in Binary Stars*, ed. R. A. M. J. Wijers, M. B. Davies, & C. A. Toot (Dordrecht: Kluwer), 141
 Livio, M., & Soker, N. 1988, *ApJ*, 329, 764
 Lombardi, J. C., Rasio, F. A., & Shapiro, S. L. 1996, in preparation
 Meyer, F., & Meyer-Hofmeister, E. 1979, *A&A*, 78, 167
 Monaghan, J. J. 1992, *ARA&A*, 30, 543
 Ostriker, J. P. 1975, in *IAU Symp. 73, The Structure and Evolution of Close Binary Systems*, ed. P. Eggleton, S. Mitton, & J. Whelan (Dordrecht: Reidel)
 Paczyński, B. 1976, in *The Structure and Evolution of Close Binary Systems*, ed. P. Eggleton, S. Mitton, & J. Whelan (Dordrecht: Reidel), 75
 Rasio, F. A. 1991, Ph.D. thesis, Cornell Univ.
 ———. 1996, in *NATO ASI on Evolutionary Processes in Binary Stars*, ed. R. A. M. J. Wijers, M. B. Davies, & C. A. Toot (Dordrecht: Kluwer), 121
 Rasio, F. A., & Shapiro, S. L. 1991, *ApJ*, 377, 559
 ———. 1992, *ApJ*, 401, 226
 ———. 1994, *ApJ*, 432, 242
 ———. 1995, *ApJ*, 438, 887
 Regös, E., & Tout, C. A. 1995, *MNRAS*, 273, 146
 Sawada, K., Hachisu, I., & Matsuda, T. 1984, *MNRAS*, 206, 673
 Sawada, K., Matsuda, T., & Hachisu, I. 1986, *MNRAS*, 219, 75
 Tassoul, J. 1978, *Theory of Rotating Stars* (Princeton: Princeton Univ. Press)
 Taam, R. E., & Bodenheimer, P. 1991, *ApJ*, 373, 246
 Taam, R. E., Bodenheimer, P., & Rozycka, M. 1994, *ApJ*, 431, 247
 Terman, J. L., Taam, R. E., & Hernquist, L. 1994, *ApJ*, 422, 729
 ———. 1995, *ApJ*, 445, 367
 Webbink, R. F. 1984, *ApJ*, 277, 355
 ———. 1988, in *Critical Observations versus Physical Models for Close Binary Systems*, ed. K. C. Leung (New York: Gordon & Breach), 403
 Yorke, H. W., Bodenheimer, P., & Taam, R. E. 1995, *ApJ*, 451, 308
 Yungelson, L. R., Tutukov, A. V., & Livio, M. 1993, *ApJ*, 418, 794